

Slow heat-driven flow in a gas of hard disks

Amit Kumar,^{1,*} Abhishek Dhar,^{1,†} and Baruch Meerson^{2,‡}

¹*International Centre for Theoretical Sciences, Tata Institute of Fundamental Research, Bangalore 560089, India*

²*Racah Institute of Physics, Hebrew University of Jerusalem, Jerusalem 91904, Israel*

We study a slow heat-driven flow in a gas of elastically colliding hard disks confined to a long channel. The initial state consists of two regions with large temperature and density contrasts but nearly equal pressures, leading to a low-Mach-number, nearly isobaric evolution. In the dilute limit, the corresponding isobaric hydrodynamic theory reduces to a previously known ideal-gas description. We extend this theory to finite densities by incorporating a non-ideal equation of state of a hard-disk fluid, and solve the resulting one-dimensional equations numerically. Finite-density effects produce appreciable deviations from the ideal-gas prediction. We then test the theory directly against event-driven molecular dynamics simulations of hard disks and find very good agreement in both the dilute and finite-density regimes. The results provide, to our knowledge, the first particle-level test of isobaric gas dynamics of a strongly inhomogeneous cooling flow.

I. INTRODUCTION

Gas dynamics is governed by the conservation laws of mass, momentum, and energy, which together form the compressible Navier–Stokes equations. In many physically relevant situations, however, the characteristic time scale of interest is long compared to the acoustic time, so that sound waves rapidly establish mechanical equilibrium. In the absence of external forces this corresponds to an approximately uniform pressure, whereas in the presence of gravity it corresponds to an approximately hydrostatic state. The resulting asymptotic reduction filters out acoustic dynamics while retaining the slow evolution of temperature, density, and velocity fields. Such flows are commonly referred to as low-Mach-number or zero-Mach-number flows.

The zero-Mach-number approximation has been developed in a variety of contexts, including thermally driven flows, combustion, and atmospheric dynamics [1–7]. In these systems the separation of time scales between fast acoustic propagation and slow thermal evolution leads to an approximately isobaric late-time dynamics. During this late-time evolution, the hydrodynamic velocity in the region of interest remains small compared to the speed of sound, but substantial spatial variations of temperature and density can still give rise to a strongly nonlinear dynamics.

An important class of problems within this framework is slow relaxation of strongly nonuniform temperature fields. In such systems, the dynamics is driven primarily by heat transport and the associated density variations, while the pressure remains nearly uniform, and the flow speed is small compared to the speed of sound, thus implying low Mach-number. Earlier work has shown that strongly heated localized regions can exhibit nontrivial cooling dynamics and self-similar behav-

ior [8–12]. These results demonstrated that the zero-Mach-number regime is not limited to weak perturbations, but can also describe strongly nonlinear processes. Low-Mach-number regimes also arise in granular gases [13–15], where weakly-inelastic collisions add a bulk cooling term to the energy equation, and in other systems.

Despite the broad use of hydrodynamic descriptions, connecting them quantitatively to underlying microscopic dynamics remains an important problem. Rigorous derivations are scarce, and direct numerical tests have mainly been carried out for strongly compressible, rapidly evolving flows, with much less attention to slow, thermally driven regimes. In particular, recent studies employing molecular dynamics of hard-particle systems have enabled direct comparisons between microscopic dynamics and hydrodynamic predictions in such high-Mach-number settings. These works have demonstrated quantitative agreement even in strongly nonequilibrium situations such as blast-wave evolution [16–26], while also revealing the coexistence of hydrodynamic regions with non-hydrodynamic structures, thereby delineating both the predictive power and the limitations of continuum descriptions.

The above studies have primarily focused on fast, strongly compressible processes characterized by large Mach numbers, where shock formation and inertial effects dominate the dynamics. In contrast, much less attention has been given to direct microscopic tests of hydrodynamic behavior in slow, thermally driven flows in the limit of small Mach number. In this regime, pressure is effectively equilibrated, and the dynamics is governed by an interplay between heat transport, density variations, and weak hydrodynamic motion. The extent to which the zero-Mach-number hydrodynamic description emerges from microscopic dynamics in such strongly nonlinear situations remains largely unexplored.

In this work, we address this gap by considering an isobaric heat-driven flow of a gas in a geometrically simple setting: a long, narrow channel in which the macroscopic flow is effectively one-dimensional. The initial state consists of two regions with markedly different temperatures and densities but nearly equal pressures, leading to a

* getkamit@gmail.com

† abhishek.dhar@icts.res.in

‡ meerson@mail.huji.ac.il

strongly nonlinear yet nearly isobaric evolution. While the dilute-gas limit provides the direct counterpart of the ideal-gas theory of Ref. [8], we also extend the analysis and simulations to finite densities, where deviations from ideal-gas behavior become important. This setup allows for a transparent theoretical analysis of the nonlinear evolution under the isobaric constraint. It is also well suited for direct numerical investigation using event-driven molecular dynamics of elastically colliding hard disks, thus providing a microscopic realization of the gas dynamics.

The present study provides a direct particle-level test of zero-Mach-number hydrodynamics in the nearly isobaric heat-driven flow considered here. In doing so, it extends earlier microscopic tests of hydrodynamic behavior from high-Mach-number regimes to the opposite limit of slow, nearly isobaric dynamics. More broadly, it adds to the evidence that continuum hydrodynamics can accurately describe far-from-equilibrium gas dynamics across widely different time scales and flow regimes.

The remainder of the paper is organized as follows. In Sec. II we summarize the formalism [8] for the isobaric heat-driven flow of an ideal gas and specialize it to the one-dimensional setting described above. In Sec. III, we extend the formalism to the finite density case and derive the relevant hydrodynamic scaling equations, while in Sec. IV we discuss their solutions. In Sec. V we describe our event-driven molecular dynamics simulations and compare the theoretical predictions with the simulation results. Section VI presents a brief discussion of our results.

II. ISOBARIC HEAT-DRIVEN FLOW OF IDEAL GAS

Consider a long channel filled with ideal gas. The initial temperature and density of the gas is T_L and ρ_L at $x < 0$, T_R and ρ_R at $x > 0$. As we want to study a zero-Mach-number heat-conduction process, we choose the parameters T_L, T_R, ρ_L and ρ_R to obey the relation

$$\rho_L T_L = \rho_R T_R, \quad (1)$$

so that the ideal gas pressure is constant through the system.

We will follow the evolution of the temperature and density of the gas over times much longer than the typical sound travel time through the system. The basic process here is heat transfer from the hot part of the gas to the cold part. Importantly, the gas density also changes: there is a slow flow of the gas from the dense (cold) to dilute (hot) region so that the pressure over the system remains approximately constant. This implies that the density profile is “slaved” by the temperature profile (or vice versa), so that

$$\rho(x, t)T(x, t) \simeq \text{const.} \quad (2)$$

at all times.

The governing equation for the temperature is a planar analog of the nonlinear heat equation [8] originally derived for a study of the isobaric cooling flow which develops after a strong explosion in a gas. In the present one-dimensional setting the equation has the form

$$\partial_t T = \beta_0 T^2 \partial_x \left(T^{-1/2} \partial_x T \right). \quad (3)$$

The dimensional coefficient β_0 is defined by the relation

$$\beta(T) \equiv \frac{\kappa(T)}{c_p \rho_R T_R} \equiv \beta_0 T^{1/2}, \quad (4)$$

where $\kappa(T) \sim T^{1/2}$ and c_p are the heat conductivity and the isobaric heat capacity of ideal gas, respectively.

Once the temperature $T(x, t)$ is determined, one can calculate the gas density $\rho(x, t) = \rho_R T_R / T(x, t)$ and the heat-driven flow velocity [8]

$$v(x, t) = \beta_0 T^{1/2} \partial_x T. \quad (5)$$

In our one-dimensional setting Eq. (3) should be solved subject to the boundary conditions

$$T(x = -\infty, t) = T_L \quad \text{and} \quad T(x = \infty, t) = T_R \quad (6)$$

and the initial condition

$$T(x, 0) = T_L + (T_R - T_L) \theta(x), \quad (7)$$

where $\theta(x)$ is the Heaviside step-function.

Since the formulation of this problem does not include any quantity with the dimension of length, the solution is self-similar starting from $t = 0$, and the similarity ansatz immediately follows from dimensional analysis [27]. The dimensions of β_0 can be found from Eq. (3):

$$[\beta_0] = \frac{\text{length}^2}{\text{time} \times \text{temperature}^{3/2}}. \quad (8)$$

This leads to the similarity ansatz

$$T(x, t) = T_R \Theta \left[\frac{x}{T_R^{3/4} (\beta_0 t)^{1/2}} \right]. \quad (9)$$

Plugging it into Eq. (3), we obtain an ordinary differential equation (ODE) for the scaling function $\Theta(\xi)$:

$$\Theta^2 \frac{d}{d\xi} \left(\Theta^{-1/2} \frac{d\Theta}{d\xi} \right) + \frac{\xi}{2} \frac{d\Theta}{d\xi} = 0. \quad (10)$$

This ODE should be solved subject to the boundary conditions $\Theta(-\infty) = T_L/T_R$ and $\Theta(\infty) = 1$. For a given T_L/T_R the solution for the scaling function $\Theta(\xi)$ can be obtained numerically by the shooting method [28]. Two examples of numerically found $\Theta(\xi)$ are shown in Fig. 1.

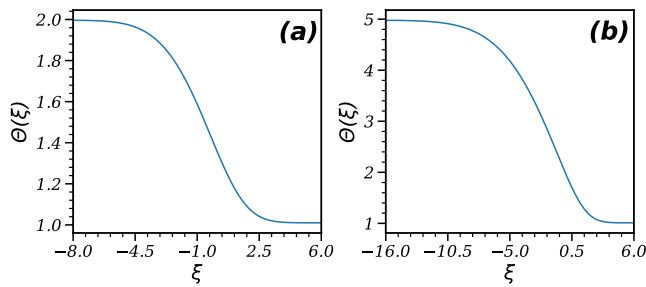


FIG. 1. Scaling function $\Theta(\xi)$ for $T_L/T_R = 2$ (left panel) and 5 (right panel).

III. ISOBARIC HEAT-DRIVEN FLOW AT FINITE DENSITY

Going over to finite densities, we again fill the two halves of the long and narrow channel with hard-disk gas at different temperatures T_L and T_R and densities ρ_L and ρ_R , but at the same constant pressure p_0 . At finite densities, the pressure of such a gas obeys the non-ideal equation of state

$$p = \rho T Z(\rho), \quad (11)$$

where $Z(\rho)$ is given in terms of the virial expansion and can be approximated by the Henderson form for hard disks each having unit diameter [29],

$$Z(\rho) = \frac{128 + \pi^2 \rho^2}{8(4 - \pi \rho)^2}. \quad (12)$$

Therefore, the initial conditions obey the relations $\rho_L T_L Z(\rho_L) = \rho_R T_R Z(\rho_R) = p_0$.

The macroscopic dynamics of this quasi-one-dimensional finite-density gas is described by one-dimensional Navier-Stokes equations for the gas density $\rho(x, t)$, velocity $v(x, t)$, and temperature $T(x, t)$ or equivalently the pressure $p(x, t)$ [30, 31]. Since we will focus on low Mach number flows, viscous effects can be neglected, and we obtain

$$\partial_t \rho + \partial_x(\rho v) = 0, \quad (13a)$$

$$\rho(\partial_t v + v \partial_x v) + \partial_x p = 0, \quad (13b)$$

$$\rho c_v (\partial_t T + v \partial_x T) + p \partial_x v = \partial_x (\kappa \partial_x T), \quad (13c)$$

where $c_v = 1/(\gamma - 1)$ is the specific heat at constant volume, $\gamma = 2$ for a two-dimensional monoatomic gas, and p is given by Eq. (11). Finally, κ in Eq. (13c) is the thermal conductivity of the hard-disk gas [32, 33],

$$\kappa = C_1 \sqrt{T}. \quad (14)$$

The coefficient C_1 is known from the Chapman-Enskog expansion [34–37], and, at the lowest order, is independent of ρ . The lowest-order Chapman-Enskog value is given by $C_1^* = 2/\sqrt{\pi}$ for hard disk of unit diameter. It is known, however, that in two dimensions, hydrodynamic

long-time tails can lead to a logarithmic system-size dependence of transport coefficients [38–40]. However, the bare transport coefficients, defined on kinetic scales, are finite and the slow divergence at hydrodynamic scales is not expected to affect the nonequilibrium dynamics. Nevertheless there is some uncertainty about the value of the coefficient C_1 . In view of this we will use the coefficient C_1 as the single adjustable parameter in making our comparisons of the hydrodynamic predictions and molecular dynamics simulations.

The hydrodynamic equations should be supplemented by the boundary conditions

$$T(x \rightarrow -\infty, t) = T_L, \quad T(x \rightarrow \infty, t) = T_R, \quad (15a)$$

$$\rho(x \rightarrow -\infty, t) = \rho_L, \quad \rho(x \rightarrow \infty, t) = \rho_R. \quad (15b)$$

$$v(x \rightarrow -\infty, t) = 0, \quad v(x \rightarrow \infty, t) = 0. \quad (15c)$$

Under the low Mach-number approximation, the momentum equation (13b) can be replaced by the isobaricity condition,

$$p = \rho T Z(\rho) \simeq p_0 = \text{const}, \quad (16)$$

thus reducing the number of independent fields by one. As a result, we can focus on the Eqs. (13a), (13c) and (16). These equations, with an initial condition and proper boundary conditions, determine the hydrodynamic flow completely. Further, since the temperature and density jump at $t = 0$ does not have a length scale, the thermal spreading of this jump is described by a self-similar solution which we will now determine. By comparing Eq. (4) and Eq. (14), we get $\beta_0 = C_1/(c_p \rho_R T_R)$. Further, using Eq. (13c), we identify the constant $D = C_1 T_R^{1/2}/(c_p \rho_R) \equiv \beta_0 T_R^{3/2}$ with dimensions of a diffusion coefficient, $\text{length}^2/\text{time}$. With this parameter, we can define a diffusive scaling variable $\xi = x/\sqrt{Dt}$. As a result, the hydrodynamic fields exhibit the same self-similarity and diffusive scaling as in the dilute limit:

$$\frac{\rho}{\rho_R} = R(\xi), \quad v = \frac{\sqrt{D}}{\sqrt{t}} V(\xi), \quad \frac{T}{T_R} = \Theta(\xi). \quad (17)$$

Plugging these scaling forms in Eqs. (13a) and (13c) we obtain two coupled nonlinear ODEs for the scaling functions R, V and Θ :

$$\left(V - \frac{\xi}{2}\right) \frac{\partial R}{\partial \xi} + R \frac{\partial V}{\partial \xi} = 0, \quad (18)$$

$$R \left(V - \frac{\xi}{2}\right) \frac{\partial \Theta}{\partial \xi} + \bar{p}_0 \frac{\partial V}{\partial \xi} = \gamma \frac{\partial}{\partial \xi} \left(\Theta^{1/2} \frac{\partial \Theta}{\partial \xi}\right), \quad (19)$$

where $\bar{p}_0 = p_0/(c_v \rho_R T_R)$ is the rescaled constant pressure. Using the isobaricity condition (16), which becomes

$$p_0 = \rho_R T_R R(\xi) \Theta(\xi) Z(\rho_R R(\xi)), \quad (20)$$

we can reduce Eqs. (18) and (19) to two coupled ODEs for the scaling functions R and V . These ODEs should be solved with the boundary conditions

$$R(\infty) = 1, \quad R(-\infty) = \frac{\rho_L}{\rho_R}, \quad V(\infty) = 0. \quad (21)$$

The problem can be solved numerically by the shooting method [28]. In the next two sections we will obtain such numerical solutions and compare them with results from molecular dynamic simulations.

In the dilute limit, where $Z(\rho) = 1$, one can recover from this formulation Eq. (10). The simplification comes from the fact that for $Z(\rho) = 1$, $v(x, t)$ becomes proportional to the heat flux. Under isobaricity, this leads to a single equation either for the temperature, or for the density [8].

IV. FINITE-DENSITY SOLUTIONS

The rescaled equation (10) for ideal gas is parameter-free. The solutions of this equation depend only on the density ratio ρ_L/ρ_R and are independent of the gas pres-

sure. The solutions of the rescaled finite-density equations (18) and (19) do depend on the pressure. This effect is clearly seen in Fig. 2, where we compare the rescaled density, velocity, and temperature profiles, obtained from the numerical solution of Eqs. (18) and (19), for three pressure values: $p_0 = 5, 10$, and 20 . We observe that increasing the pressure broadens the transition region and increases the magnitude of the negative velocity peak.

We next examine the dependence of the finite-density solution on ρ_L/ρ_R . In Fig. 3 we plot the rescaled density, velocity, and temperature profiles for three different values of this ratio: $\rho_R = 3\rho_L/2, 2\rho_L$, and $5\rho_L/2$, while keeping the remaining parameters fixed. We find that increasing ρ_R leads to steeper density and temperature profiles. At the same time, the magnitude of the negative velocity peak increases, and its position shifts to the left.

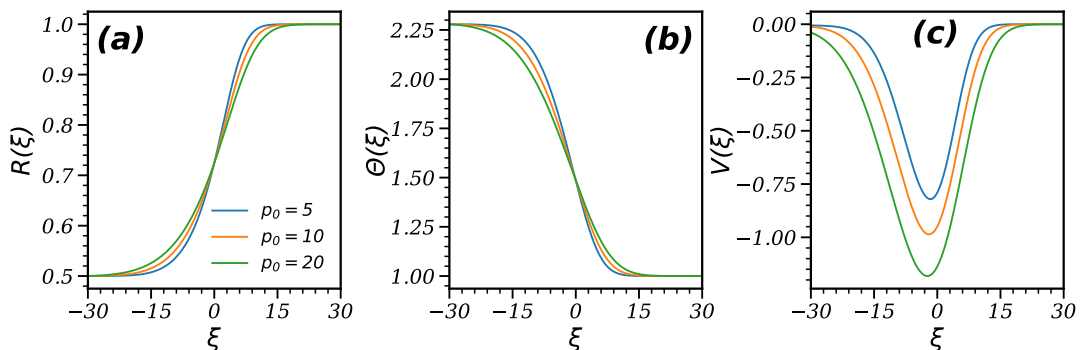


FIG. 2. Dependence of the NSE solution on the initial pressure p_0 : Rescaled density R (a), velocity V (b), and temperature Θ (c) as functions of the rescaled coordinate ξ , obtained from numerical solution of Eqs. (18) and (19) for pressures $p_0 = 5, 10$, and 20 . As the pressure increases, the transition region broadens, and the magnitude of the negative velocity peak increases. The parameters are $\rho_L = 0.075$, $\rho_R = 0.15$, $T_R = p_0/[\rho_R Z(\rho_R)]$, and $T_L = p_0/[\rho_L Z(\rho_L)]$.

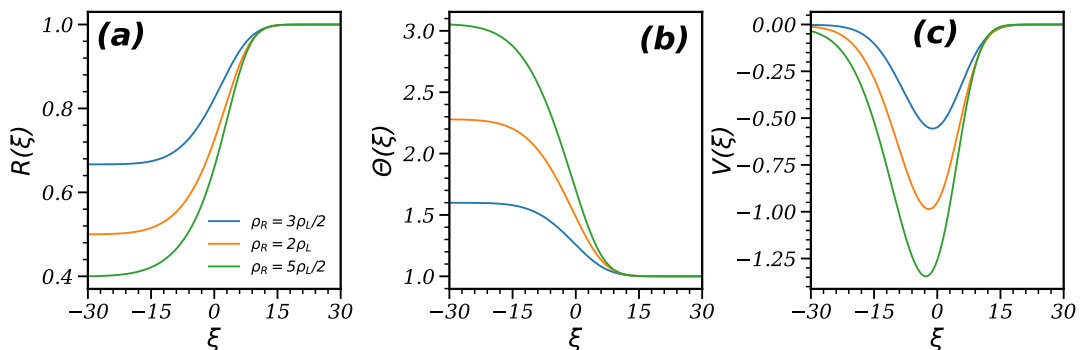


FIG. 3. Dependence of the finite-density solution on the density ratio ρ_R/ρ_L : Shown are the rescaled density R (a), velocity V (b), and temperature Θ (c) as functions of the rescaled coordinate ξ , obtained from the numerical solution of Eqs. (18) and (19) for $\rho_R = 3\rho_L/2, 2\rho_L$, and $5\rho_L/2$, with $\rho_L = 0.075$. As ρ_R increases, the density and temperature profiles become steeper, while the magnitude of the negative velocity peak increases, and its position shifts to the left. The parameters are: $p_0 = 10$, $T_R = p_0/[\rho_R Z(\rho_R)]$, and $T_L = p_0/[\rho_L Z(\rho_L)]$.

In the dilute limit, $(\rho_L, \rho_R) \rightarrow (0, 0)$, the finite-density hard-disk gas is expected to approach ideal-gas behavior. To demonstrate this, in Fig. 4 we compare the finite-density numerical solutions with those obtained for an ideal gas under the same initial conditions. Specifically, we consider two sets of high and low initial densities: $(\rho_L, \rho_R) = (0.075, 0.15)$ [Fig. 4(a-c)] and $(\rho_L, \rho_R) =$

$(0.005, 0.01)$ [Fig. 4(d-f)]. We observe that, for larger densities, the solutions for the ideal gas and finite-density gas exhibit noticeable differences [see Fig. 4(b)]. However, as the initial densities are reduced, the corresponding profiles for the two systems become closer [see Fig. 4(e-f)], as to be expected.

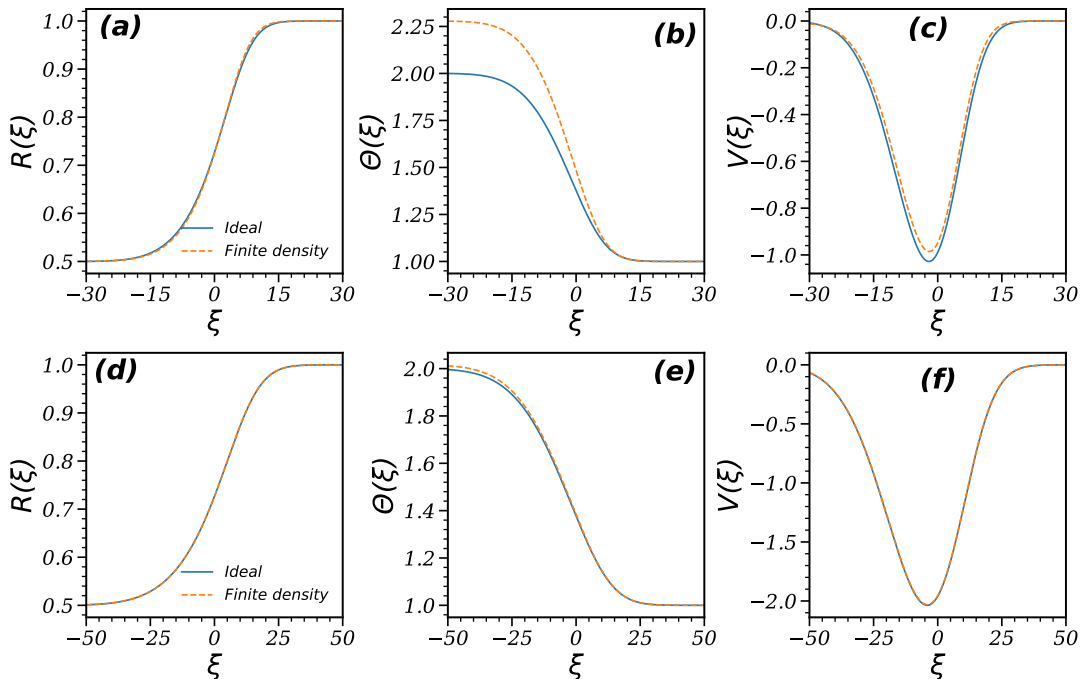


FIG. 4. Finite-density hard disk gas vs. ideal gas. Shown are the rescaled density R , velocity V , and temperature Θ as functions of the rescaled coordinate ξ , obtained from the numerical solution of Eqs. (18) and (19). Panels (a-c) correspond to the initial densities $\rho_L = 0.075$ and $\rho_R = 0.15$, while panels (d-f) correspond to $\rho_L = 0.005$ and $\rho_R = 0.01$. The ideal-gas results are obtained by setting the compressibility factor $Z(\rho) = 1$. It is evident from the plots that, as the initial densities become very small, the finite-density solution and the ideal-gas solutions converge. The parameters are: $p_0 = 10$, $T_R = p_0/[\rho_R Z(\rho_R)]$, and $T_L = p_0/[\rho_L Z(\rho_L)]$.

V. MOLECULAR DYNAMICS SIMULATIONS

We now describe the event-driven molecular dynamics (EDMD) simulations we used to model the system. We consider N identical hard disks, labeled $i = 1, 2, \dots, N$, confined in a long two-dimensional channel of dimensions $L \times W$, with $L \gg W$. Each particle has unit mass and unit diameter. The initial particle velocities are sampled from Maxwell distributions corresponding to different temperatures T_L and T_R in the left and right halves, respectively. The densities ρ_L and ρ_R in the left and right halves of the channel are chosen such that the entire channel is at a uniform pressure p_0 .

The system evolves through a sequence of momentum and energy-conserving elastic collisions, including both particle-particle and particle-wall interactions. The sim-

ulations are carried out using an event-driven molecular dynamics scheme, in which the system evolves from one event to the next [41].

To characterize the system, we measure coarse-grained fields: the density, velocity, temperature, and pressure. The local density $\rho(\vec{r}, t)$ and velocity $v(\vec{r}, t)$ are defined as averages over particles within a small spatial region around position \vec{r} at time t . The local temperature $T(\vec{r}, t)$ is defined as the variance of local velocity. The local pressure for a hard disk system is computed using the virial expression [42]

$$p = \rho T - \frac{\rho}{2N'\Delta t'} \sum_{\text{collisions}} \vec{r}_{ij} \cdot \vec{v}_{ij}, \quad (22)$$

where $\vec{r}_{ij} = \vec{r}_i - \vec{r}_j$ is the separation vector at collision, \vec{v}_{ij} is the relative velocity, $\Delta t'$ is the averaging time in-

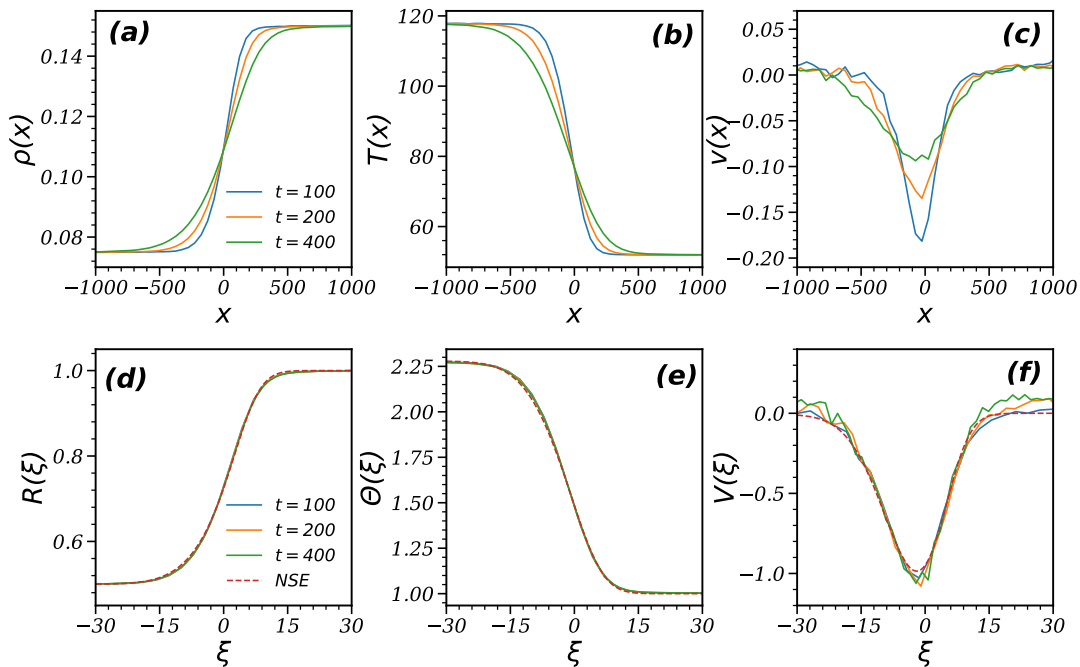


FIG. 5. Spatio-temporal behavior of (a–c) density, temperature, and velocity as functions of x at different times $t = 100, 200, 400$, and (d–f) the scaled functions and comparison with the hydrodynamic predictions. The solid lines in Figs. (a–f) represent the EDMD data, and the dashed lines in Figs. (e–f) represent the solution of Eqs. (18) and (19). We see that the MD data shows good scaling collapse in accordance with the scaling ansatz Eq. (17). The results are shown for the parameters: $p_0 = \rho T Z(\rho) = 10$, $\rho_R = 0.15$, $\rho_L = 0.075$, $T_R = p_0 / [\rho_R Z(\rho_R)]$, and $T_L = p_0 / [\rho_L Z(\rho_L)]$. The typical simulation box for these parameters was $L = 10^4$ and $W = 10$ with the total of $N = 11,250$ hard disks. The data are averaged over 2.1×10^5 initial configurations. The corresponding speeds of sound are ≈ 17.3 on the left side and ≈ 13 on the right side. The adjustable parameter C_1 in the heat conductivity $\kappa = C_1 \sqrt{T}$ is taken to be $C_1 = 0.13$.

terval, and N' is the average number of particles within the spatial bin used for the measurement.

Now we present the simulation results for the parameters $\rho_R = 0.15$, $\rho_L = 0.075$, $v_L = v_R = 0$, and $p_0 = 10$. In Figs. 5(a–c), we plot the three hydrodynamic fields as functions of x at different times, $t = 100, 200, 400$. The gradual broadening of the transition region with time is clearly observed.

Next, we compare our isobaric hydrodynamic solution for the finite-density gas of hard disks, presented in Sec. IV, with the molecular dynamics simulations. In Figs. 5(d–f), we plot the rescaled density, velocity, and temperature profiles as functions of the rescaled variable ξ . We observe an excellent collapse the EDMD data obtained at different times $t = 100, 200, 400$, and very good agreement between the EDMD results and the isobaric hydrodynamic solutions. We find the best agreement for $C_1 = 0.12$, which enters the rescaled coordinate ξ through the diffusion constant D .

In Fig. 6, we show the results of pressure measurements from EDMD, as given in Eq. (22). We see that the pressure indeed remains nearly constant and equal to the initial pressure $p_0 = 10$. Although at $t = 400$ the pressure perturbation has already reached the boundaries of the channel in the x -direction, the reflected waves do not affect the region $|x| \leq 2000$. Therefore, it remains jus-

tified to compare the thermodynamic fields at $t = 400$, since the transition region is still well confined within $|x| \leq 1000$.

VI. SUMMARY AND DISCUSSION

We have studied the late-time, isobaric heat-driven flow of a gas of hard disks in a long channel in the low-Mach-number regime. In this regime the pressure remains nearly constant throughout the system, which makes it possible to replace the full compressible hydrodynamic equations by an isobaric description, in which the temperature and density fields evolve nonlinearly subject to the constraint of mechanical equilibrium.

The theoretical formulation used here is the one-dimensional version of the isobaric heat-conduction formalism. In the dilute limit it reduces to the ideal-gas description [8], with the hard-disk heat conductivity entering as the transport coefficient. We solved the resulting equations numerically for the initial condition consisting of two regions with large temperature and density contrasts but nearly equal pressures. This setting provides a simple example of strongly nonlinear thermal relaxation in which the hydrodynamic velocity remains small compared with the sound speed.

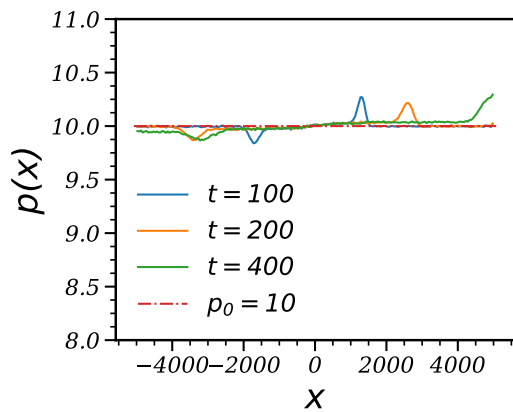


FIG. 6. Spatio-temporal behavior of the pressure vs. x at three different times. The solid lines represent the EDMD data at times $t = 100$, 200 , and 400 , while the dashed horizontal line serves as a guide to the eye indicating the initial pressure $p_0 = 10$. As one can see, the system remains nearly isobaric throughout at all times. The results are shown for the parameters $p_0 = \rho T Z(\rho) = 10$, $\rho_R = 0.15$, $\rho_L = 0.075$, $T_R = p_0 / [\rho_R Z(\rho_R)]$, and $T_L = p_0 / [\rho_L Z(\rho_L)]$. For these parameters we used $L = 10^4$ and $W = 10$ with the total number of $N = 11,250$ hard disks. The data are averaged over 2.1×10^5 initial configurations. The corresponding speeds of sound are $\simeq 17.3$ on the left side and ≈ 13 on the right side.

We also extended the hydrodynamic calculation beyond the dilute-gas limit by using a finite-density equation of state for hard disks. The finite-density corrections modify the relation between density, temperature, and pressure, and therefore affect the subsequent heat and mass redistribution. Our results show that these corrections are already appreciable at the moderate densities considered here. In particular, the finite-density theory gives a noticeably different evolution from the ideal-gas approximation, demonstrating that non-ideal equation-of-state effects must be retained for quantitative comparison with simulations outside the dilute limit.

The hydrodynamic predictions were then tested

against event-driven molecular dynamics simulations of elastically colliding hard disks. The comparison shows very good agreement between the continuum theory and the particle simulations, both in the dilute-gas limit and at finite densities. This agreement includes the evolution of the temperature and density profiles and the associated slow mass redistribution along the channel. The simulations therefore provide a direct microscopic test of the isobaric low-Mach-number description in a strongly inhomogeneous, thermally driven flow.

The present results complement earlier particle-level tests of hydrodynamics in rapidly evolving, high-Mach-number settings such as blast-wave dynamics. Here the relevant regime is the opposite one: the pressure equilibrates rapidly, the flow velocity is small, and the dynamics is controlled by heat conduction and the corresponding density adjustment. The agreement between theory and simulation shows that the zero-Mach-number reduction can emerge accurately from microscopic hard-disk dynamics, not only in the ideal dilute limit but also when finite-density corrections to the equation of state are important.

In conclusion, a combination of low-Mach-number theory, finite-density hard-disk thermodynamics, and event-driven simulations provides a controlled microscopic realization of nonlinear isobaric heat driven flow.

Acknowledgments. We thank the Rutgers Mathematical Physics Webinar series, organized by Joel Lebowitz, which led to this collaboration. All the simulations were carried out on Supercomputers Contra, Tetris, and Mario at ICTS-TIFR Bengaluru. A.K. and A.D. would like to acknowledge the support from the DAE, Government of India, under Project No. RTI4001. AD acknowledges the J.C. Bose Fellowship (JCB/2022/000014) of the Science and Engineering Research Board of the Department of Science and Technology, Government of India. B.M. was supported by the Israel Science Foundation (Grant No. 1579/25).

-
- [1] R. G. Rehm and H. R. Baum, *J. Res. Natl. Bur. Stand.* **83**, 297 (1978).
 - [2] A. Majda and J. Sethian, *Combust. Sci. Technol.* **42**, 185 (1985).
 - [3] A. Majda, *Compressible Fluid Flow and Systems of Conservation Laws in Several Space Variables* (Springer Science & Business Media, 2012).
 - [4] F. A. Williams, *Combustion Theory*, 2nd ed. (Benjamin Cummings, Menlo Park, CA, 1985) p. 445.
 - [5] T. Poinsot and D. Veynante, *Theoretical and Numerical Combustion* (RT Edwards, Inc., 2005).
 - [6] Y. Ogura and N. A. Phillips, *J. Atmos. Sci.* **19**, 173 (1962).
 - [7] D. R. Durran, *J. Atmos. Sci.* **46**, 1453 (1989).
 - [8] B. Meerson, *Phys. Fluids A* **1**, 887 (1989).
 - [9] D. Kaganovich, B. Meerson, A. Zigler, C. Cohen, and J. Levin, *Phys. Plasmas* **3**, 631 (1996).
 - [10] A. Glasner, E. Livne, and B. Meerson, *Phys. Rev. Lett.* **78**, 2112 (1997).
 - [11] B. Meerson, P. V. Sasorov, and K. Sekimoto, *Phys. Rev. E* **61**, 1403 (2000).
 - [12] S. Kamin and L. Dascal, in *Optimal Control and Partial Differential Equations*, edited by J. L. Menaldi, E. Rofman, and A. Sulem (IOS Press, Amsterdam, 2001) pp. 171–180.
 - [13] I. Goldhirsch, *Annu. Rev. Fluid Mech.* **35**, 267 (2003).
 - [14] Y. Bromberg, E. Livne, and B. Meerson, in *Granular Gas Dynamics*, Lecture Notes in Physics, Vol. 624, edited by T. Pöschel and N. Brilliantov (Springer, Berlin, 2003) pp. 251–266.

- [15] D. Volfson, B. Meerson, and L. S. Tsimring, Phys. Rev. E **73**, 061305 (2006).
- [16] J. P. Joy, S. N. Pathak, and R. Rajesh, J. Stat. Phys. **182**, 1 (2021).
- [17] J. P. Joy and R. Rajesh, J. Stat. Phys. **184**, 1 (2021).
- [18] S. Chakraborti, S. Ganapa, P. L. Krapivsky, and A. Dhar, Phys. Rev. Lett. **126**, 244503 (2021).
- [19] S. Ganapa, S. Chakraborti, P. L. Krapivsky, and A. Dhar, Phys. Fluids **33**, 087113 (2021).
- [20] S. Chakraborti, A. Dhar, and P. Krapivsky, SciPost Phys. **13**, 074 (2022).
- [21] A. Kumar and R. Rajesh, J. Stat. Phys. **188**, 1 (2022).
- [22] S. K. Singh, S. Chakraborti, A. Dhar, and P. L. Krapivsky, J. Stat. Phys. **190**, 118 (2023).
- [23] A. Kumar and R. Rajesh, J. Stat. Phys. **192**, 121 (2025).
- [24] A. Kumar and R. Rajesh, J. Stat. Phys. **192**, 17 (2025).
- [25] A. Kumar and R. Rajesh, J. Stat. Phys. **192**, 119 (2025).
- [26] U. Kumar, A. Dhar, and P. Krapivsky, J. Stat. Mech. Theory Exp. **2026**, 023216 (2026).
- [27] G. I. Barenblatt, *Scaling, Self-similarity, and Intermediate Asymptotics: Dimensional Analysis and Intermediate Asymptotics* (Cambridge University Press, Cambridge, UK, 1996).
- [28] J. Stoer and R. Bulirsch, *Introduction to Numerical Analysis* (Springer-Verlag, New York, 1980).
- [29] A. Barrat and E. Trizac, Phys. Rev. E **66**, 051303 (2002).
- [30] L. D. Landau and E. M. Lifshitz, *Fluid Mechanics, Course of Theoretical Physics, Vol. 6* (Butterworth-Heinemann, Oxford, UK, 1987).
- [31] Z. U. A. Warsi, *Fluid Dynamics: Theoretical and Computational Approaches* (CRC Press, 2005).
- [32] K. Huang, *Statistical Mechanics* (John Wiley & Sons, 2008).
- [33] F. Reif, *Fundamentals of Statistical and Thermal Physics* (Waveland Press, 2009).
- [34] J. R. Dorfman, H. van Beijeren, and T. R. Kirkpatrick, *Contemporary Kinetic Theory of Matter* (Cambridge University Press, 2021).
- [35] D. M. Gass, J. Chem. Phys. **54**, 1898 (1971).
- [36] R. García-Rojo, S. Luding, and J. J. Brey, Phys. Rev. E **74**, 061305 (2006).
- [37] G. M. Kremer, *An Introduction to the Boltzmann Equation and Transport Processes in Gases* (Springer Science & Business Media, 2010).
- [38] B. J. Alder and T. Wainwright, Physical review A **1**, 18 (1970).
- [39] M. Ernst, E. Hauge, and J. Van Leeuwen, Phys. Rev. Lett. **25**, 1254 (1970).
- [40] Y. Pomeau and P. Résibois, Phys. Rep. **19**, 63 (1975).
- [41] D. C. Rapaport, *The Art of Molecular Dynamics Simulation* (Cambridge University Press, 2004).
- [42] M. Isobe, Mol. Simul. **42**, 1317 (2016).